

Earth's earliest evolved crust generated in an Iceland-like setting

Jesse R. Reimink^{1*}, Thomas Chacko¹, Richard A. Stern^{1,2} and Larry M. Heaman¹

It is unclear how the earliest continental crust formed on an Earth that was probably originally surfaced with oceanic crust. Continental crust may have first formed in an ocean island-like setting, where upwelling mantle generates magmas that crystallize to form new crust. Of the oceanic plateaux, Iceland is closest in character to continental crust, because its crust is anomalously thick¹ and contains a relatively high proportion of silica-rich (sialic) rocks². Iceland has therefore been considered a suitable analogue for the generation of Earth's earliest continental crust³. However, the geochemical signature of sialic rocks from Iceland^{4–7} is distinct from the typical 3.9- to 2.5-billion-year-old Archaean rocks discovered so far⁸. Here we report the discovery of an exceptionally well-preserved, 4.02-billion-year-old tonalitic gneiss rock unit within the Acasta Gneiss Complex in Canada. We use geochemical analyses to show that this rock unit is characterized by iron enrichment, negative Europium anomalies, unfractionated rare-earth-element patterns, and magmatic zircons with low oxygen isotope ratios. These geochemical characteristics are unlike typical Archaean igneous rocks, but are strikingly similar to those of the sialic rocks from Iceland and imply that this ancient rock unit was formed by shallow-level magmatic processes that include assimilation of rocks previously altered by surface waters. Our data provide direct evidence that Earth's earliest continental crust formed in a tectonic setting comparable to modern Iceland.

Our understanding of early Earth processes is limited by the paucity of rock and mineral samples with ages greater than 3.6 billion years (Gyr). The available data come from 4.0- to 4.4-Gyr-old detrital zircon grains from Western Australia⁹ and small, scattered blocks of ancient crust, most being younger than 3.9-Gyr-old and nearly all of which have experienced multiple later magmatic or metamorphic events¹⁰. Like their younger Archaean counterparts, these ancient terranes are typically dominated by tonalite–trondhjemite–granodiorite (TTG) suite rocks, which are the main plutonic rock package of the Archaean and represent significant growth of continental crust. General geochemical characteristics of these Archaean TTGs include high Na, high Sr/Y, strong depletions in the heavy rare-earth elements (HREEs), and minor or absent Eu anomalies^{11–14}. These characteristics are best explained by partial melting of hydrated basaltic rocks at depths great enough to stabilize significant quantities of residual garnet, a high-pressure phase with an affinity for HREEs (refs 14–16). The lack of a significant Eu anomaly in TTGs indicates that plagioclase, a lower pressure mineral that incorporates Eu²⁺, had little involvement in their petrogenesis. Two main tectonic models have been proposed for the formation of Archaean TTGs and in turn early continental crust:

subduction and subsequent partial melting of the down-going oceanic slab¹⁴; and partial melting at the base of plume-generated oceanic plateaux^{17,18}. Although these models differ substantially with regard to tectonic setting, both invoke the deep-seated magmatic processes necessary to generate the geochemical features observed in TTGs. Although many detailed studies have investigated the formation of Archaean TTG suites^{11–18}, little is known regarding the nature and petrogenesis of Earth's earliest (aged > 3.9 Gyr) sialic crust and its relationship to continental crust formed later in Earth history (for example Archaean TTGs).

The Acasta Gneiss Complex (AGC), in northwestern Canada, contains the oldest known terrestrial rocks directly dated by zircon U–Pb isotope methods. The AGC comprises poly-deformed granitic to tonalitic and amphibolitic gneisses with igneous crystallization ages ranging from 4.03 to 3.40 Gyr (refs 19–22). Some units contain still older xenocrystic zircon cores up to 4.2 Gyr (refs 21,23). The various components of the AGC, like those of most ancient gneiss terranes, are typically interlayered at the decimetre to centimetre scale, making sampling of individual components difficult. Owing in part to their inherent complexity, very little whole-rock, major- and trace-element data has previously been reported for rocks of the AGC and, therefore, basic petrogenetic information is missing. Furthermore, rocks with crystallization ages > 4.0 Gyr are rare and many of the exposed rock units have significantly younger crystallization ages (~3.8–3.6 Gyr; ref. 22). However, as part of a detailed mapping campaign we have identified, from a low strain zone of the AGC, a relatively homogeneous and mappable tonalitic gneiss unit yielding abundant well-preserved igneous zircons with a U–Pb crystallization age of 4.02 Gyr (see Supplementary Methods for a discussion of the zircon U–Pb systematics). We refer to this unit as the Idiwhaa ('ancient times' in the local aboriginal language) tonalitic gneiss (ITG). This unit affords a rare opportunity to investigate directly the processes responsible for forming pre-4.0 Gyr sialic crust. To elucidate the petrogenetic history of this earliest known sample of evolved crust, we conducted whole-rock major- and trace-element analyses of the unit as well as detailed zircon U–Pb geochronology, oxygen isotope and trace-element analyses by secondary ion mass spectrometry (SIMS).

The ITG is a relatively homogeneous mafic tonalite with small, cross-cutting leucocratic veins (Supplementary Fig. 3). The ITG consists primarily of plagioclase, quartz, hornblende, biotite and minor garnet. Whole-rock major-element compositions are characterized by intermediate levels of SiO₂ (57.9–66.9 wt.%), relatively low Al₂O₃ (13.8–14.1 wt.%), high total iron (8.6–15.3 wt.% FeO_(total)) and correspondingly low Mg-numbers (100 × MgO/(MgO + FeO) = 13–18). The latter two characteristics are distinct from average Archaean TTGs (refs 12,13; 2.7 wt.% and 43, respectively)

¹Department of Earth and Atmospheric Sciences, University of Alberta, Edmonton, Alberta, T6G 2E3, Canada, ²Canadian Centre for Isotopic Microanalysis, University of Alberta, Edmonton, Alberta, T6G 2E3, Canada. *e-mail: reimink@ualberta.ca

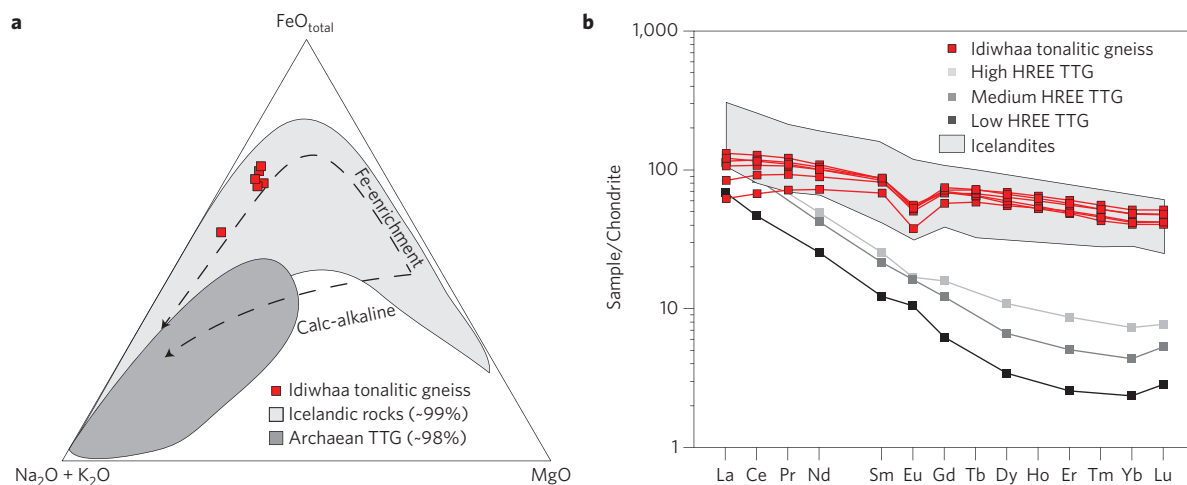


Figure 1 | Comparison of the whole-rock chemical compositions of the Idiwhaa tonalitic gneiss with Icelandic igneous rocks and Archaean TTGs.

TTG data are from ref. 2, and Icelandic data are from the GEOROC database (<http://georoc.mpch-mainz.gwdg.de/georoc/>). **a**, Major-element compositions plotted on a standard alkali-iron-magnesium diagram. The fields shown for Icelandic rocks and Archaean TTGs include 99 and 98% of the 3,763 and 1,673 total analyses, respectively. **b**, Chondrite-normalized rare-earth element (REE) plot comparing Idiwhaa tonalite data to Archaean TTGs and icelandites. The field for icelandites was extracted from the larger Icelandic database (3,763 analyses) using: SiO₂ (55–65 wt.%), Al₂O₃ (<15 wt.%) and total FeO (>8 wt.%). This left a total of 90 ‘icelandite’ analyses, 37 containing rare-earth-element data plotted here.

and indicate magma evolution along an iron-enrichment trend (Fig. 1a). These geochemical characteristics can be produced by shallow-level fractional crystallization of a relatively reduced, low-H₂O basaltic magma in which the low-pressure mineral plagioclase is a major constituent of the fractionating assemblage (along with clinopyroxene and olivine) and Fe–Ti oxide crystallization is suppressed until late in the differentiation process^{6,24}.

The whole-rock trace-element systematics of the ITG are also markedly different from average Archaean TTGs (Fig. 1b and Supplementary Fig. 4). Unlike TTGs, the REE patterns of the ITG show little fractionation of light from heavy REEs and pronounced negative Eu anomalies. These features indicate, respectively, that garnet was not involved in magma genesis or evolution, but that plagioclase fractionation played a significant role. The high-field-strength elements Zr and Hf are also elevated in the ITG relative to Archaean TTGs (ref. 12; Supplementary Fig. 3).

Given the protracted post-magmatic history of rocks of the AGC (refs 20,22), it is important to evaluate whether the whole-rock trace-element composition of this unit faithfully reflects that of its igneous precursor. The refractory mineral zircon is useful in this regard because it is strongly resistant to compositional overprinting during post-magmatic processes²⁵. Zircons extracted from one sample of the ITG, sample TC-3, are particularly well preserved and consist mainly of magmatic zircon with metamorphic overgrowths. There are two phases of magmatic zircon in the ITG that have identical U–Pb dates; unzoned cores (Phase I) and oscillatory-zoned mantles (Phase II). There are also two later phases involving either recrystallization of pre-existing zircon or new growth during metamorphism (Phases III and IV; Fig. 2a,b).

Phase I and II magmatic zircon, both of which record U–Pb ages of ~4.02 Gyr, have typical igneous zircon REE profiles that follow those predicted by equilibrium lattice strain models (Supplementary Fig. 10). Importantly, whole-rock REE profiles derived from the zircon REE data using published zircon-melt or zircon-whole-rock partition coefficients share all the key features of the measured ITG whole-rock profiles described above (Supplementary Fig. 11). This analysis confirms that igneous zircons present in the ITG were in magmatic equilibrium with a melt equivalent to the whole rock, and therefore provide a good estimate of the igneous crystallization age of the rock. It also confirms the validity of petrogenetic inferences drawn

from the whole-rock trace-element data, namely shallow- rather than deep-level processes controlled the magmatic evolution of this unit.

Oxygen isotope data also provide important insights to the petrogenesis of the ITG, in particular the role of exogenic processes in magma evolution. Here, again, zircon has the capacity to provide the most robust indication of the primary oxygen isotope composition of the magma^{25,26}. Phase I and II zircon growth zones are indistinguishable in terms of their U–Pb age but show a 0.8‰ difference in $\delta^{18}\text{O}_{\text{VSMOW}}$ values: Phase I zircon (CL-unzoned cores) has a weighted average = $+5.6 \pm 0.7\text{‰}$ (2 s.d.; $n = 62$), whereas Phase II (zoned mantles) = $+4.7 \pm 0.6\text{‰}$ (2 s.d.; $n = 66$) (Fig. 2c). The average $\delta^{18}\text{O}$ values of Phase I zircon are within the $+5.3 \pm 0.6\text{‰}$ range of zircon crystallized directly from a primary mantle melt²⁶. In contrast, Phase II zircon has $\delta^{18}\text{O}$ values below $+5\text{‰}$, which requires that the parental magma either directly assimilated, or mixed with, partial melts of low- $\delta^{18}\text{O}$ rocks that had previously undergone relatively high-temperature hydrothermal alteration by surface waters^{5,7,27,28}. Later metamorphic zircon overgrowths in the ITG (Phases III–IV) have $\delta^{18}\text{O}$ values above $+6\text{‰}$, indicating equilibration with metamorphic fluids enriched in ^{18}O (Fig. 2c). Although it appears some Phase I zircons have $\delta^{18}\text{O}$ values above the mantle zircon field (Fig. 2c), we attribute this to preferential alteration and partial resetting of the oxygen isotope systematics of a small subset of Phase I zircon by a later metamorphic fluid (see Supplementary Information for further discussion). The full oxygen isotope dataset for Phase I zircon has only a small portion of analyses outside of uncertainty of the mantle zircon field (Supplementary Fig. 12).

A petrogenetic model involving assimilation of low- $\delta^{18}\text{O}$ crust is consistent with the REE systematics of Phase I and II zircon growth zones in that the low- $\delta^{18}\text{O}$ Phase II igneous mantles have larger positive Ce anomalies than the unzoned cores (Supplementary Figs 8 and 9), suggesting the mantles crystallized under more oxidizing conditions than the cores²⁹. Such a result would be expected if the assimilated comprised rocks that had interacted with surface waters.

The Jack Hills detrital zircons from Australia with U–Pb ages up to ~4.4 Gyr have $\delta^{18}\text{O}$ values higher than those of pristine mantle zircon⁹, implying low-temperature interaction with surface waters in the Hadean. Although the ITG zircons indicate high-temperature, as opposed to low-temperature water-rock interactions, both

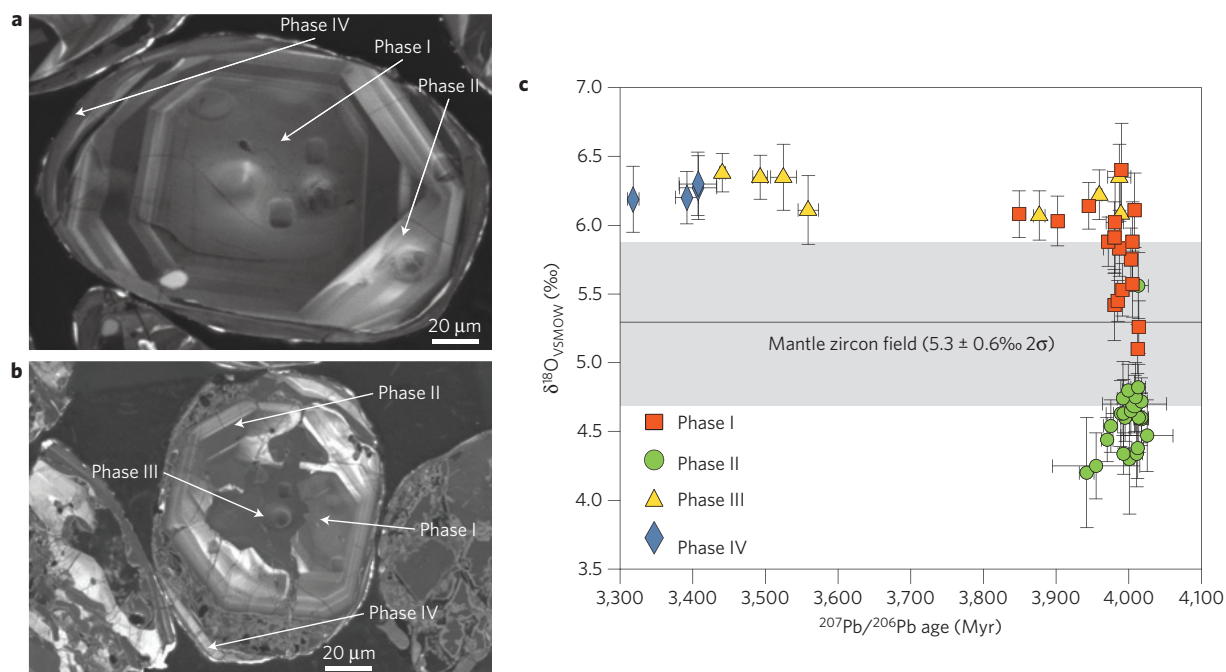


Figure 2 | Zircon phase relations and correlated zircon U-Pb and oxygen isotopic data from an Idliwhaa sample. **a, b**, Cathodoluminescence images of representative zircons in Idliwhaa tonalite sample TC-3, which show the zoning characteristics used to distinguish different phases of zircon growth. Phase I growth zones represent unzoned igneous cores. Phase II comprises fine-scale oscillatory-zoned igneous zircon, which commonly conformably overgrows Phase I zircon. Phase III growth dominantly occurs as dark metamorphic incursions grown into all earlier phases. Phase IV growth consists of metamorphic rims overgrowing all phases. **c**, Plot of $\delta^{18}\text{O}$ values (reported relative to Vienna-Standard Mean Ocean Water, VSMOW) versus $^{207}\text{Pb}/^{206}\text{Pb}$ for various zircon growth phases. The field for mantle zircon is from ref. 26. Uncertainties on all data points are shown at the 95% confidence level.

indicate the existence of a pre-4.0 Gyr hydrosphere on Earth. Cerium anomalies in the Australian detrital zircons²⁹ and ITG zircons also indicate similar magmatic oxidation states.

Although distinct from later-formed Archaean TTGs as well as igneous rocks from many modern-day tectonic settings, the geochemical features of the ITG are nearly identical to those of some intermediate rocks from Iceland (Fig. 1). In particular, a suite of rocks commonly referred to as icelandites are characterized by ~60 wt.% SiO_2 , low Al_2O_3 , high FeO, and low Mg-numbers^{4,6}. These rocks also share many of the trace-element features of the ITG, including negative Eu anomalies, little fractionation of LREE from HREE (Fig. 1b), and elevated concentrations of high-field-strength elements (Supplementary Fig. 4).

Icelandites are thought to result from some combination of low-pressure fractional crystallization of basaltic magma, hybridization of mafic and silicic magmas, and assimilation of hydrothermally altered, low- ^{18}O crust⁴⁻⁷. The latter process lowers the primary $\delta^{18}\text{O}$ values of some icelandite magmas to below pristine mantle values ($+5.5 \pm 0.5\text{‰}$; ref. 26). In this regard, low- ^{18}O magmatic rocks are relatively rare worldwide and have most commonly been documented in rift- or plume-related settings (for example, Iceland, Yellowstone, Hawaii, Skye) in which the shallow-level intrusion of hot, dry magma has produced high geothermal gradients and in turn driven hydrothermal circulation cells above the magma chambers^{5,27,28,30}.

A number of plausible tectonic scenarios have been suggested for forming sialic crust on the early Earth. We have documented the need for shallow-level fractionation of basaltic magma and assimilation of hydrothermally altered crust to generate the observed geochemical characteristics of the ~4.02 Gyr-old ITG. On the modern Earth, zones of mantle upwelling, such as plumes, rifts and ocean ridges, create the necessary conditions for generation of evolved rocks similar to the ITG. Rift- and ridge-related settings,

however, produce only a very small proportion of such rocks. In contrast, the combined thermal effects of the mid-Atlantic Ridge and a mantle plume, as well as a high degree of hydrothermal activity, has produced in Iceland a crustal thickness approaching that of typical continental crust¹, as well as a larger proportion of intermediate and felsic composition rocks (~25%; ref. 2) than in ocean ridges and other oceanic plateaux. The greater thickness and buoyancy of Icelandic-type crust makes it less susceptible to recycling back into the mantle, either in subduction zones or some other form of mantle downwelling. Therefore, we suggest that a setting similar to modern Iceland, where mantle upwelling creates a thickened plateau with a relatively high proportion of evolved rocks, would be most likely to form and preserve the ITG unit (Fig. 3).

Although the formation of Earth's earliest continental crust in an Iceland-like setting has been suggested on theoretical grounds³, no direct geological evidence supporting this hypothesis has previously been available⁸. The data presented here indicate that the oldest known sialic rock unit bears the geochemical fingerprints of shallow-level magmatic and hydrothermal processes involved in the formation of evolved Icelandic rocks. Thus, we propose that such a setting on the early Earth may have generated an analogous proto-continental crust that was sufficiently thick and buoyant to avoid later recycling into the mantle. Notably, owing to Earth's higher heat production at 4 Gyr, the confluence of a mantle plume and an ocean ridge, such as is present in modern Iceland, may not have been necessary to generate Iceland-like crust. Rather, any long-lived mantle upwelling in a planet with an operating hydrosphere may have been capable of producing the requisite conditions for formation of this type of crust. Once formed, these small continental nuclei may have served as the substrate for later, deeper-seated TTG magmatism.

Data reported here are presented in Supplementary Tables 1–8.

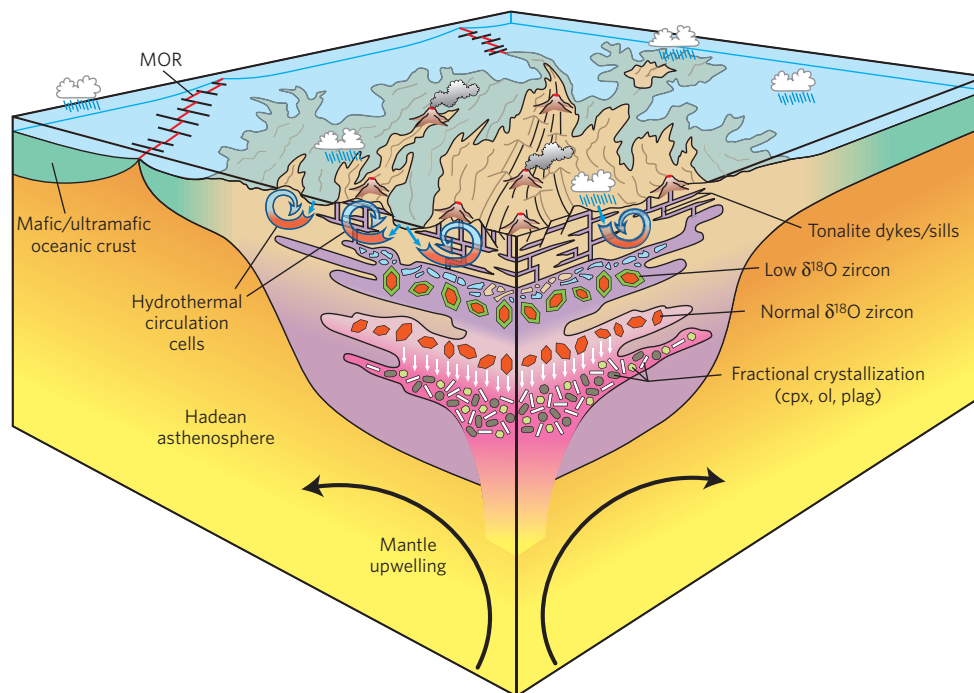


Figure 3 | Schematic diagram illustrating the major processes responsible for the formation of the Idiwhaa tonalitic gneiss. Basaltic melts are fractionated at shallow crustal levels to produce Fe-enriched intermediate magmas. These magmas initially crystallize zircon with mantle-like $\delta^{18}\text{O}$ values. Assimilation of overlying rocks that have been hydrothermally altered by surface waters lowers the $\delta^{18}\text{O}$ values of later-stage magmas and in turn produces magmatic zircon rims that have $\delta^{18}\text{O}$ values lower than those of the mantle (+5‰). All the aforementioned processes have been documented in modern-day Iceland, suggesting that Earth's earliest known sialic crust may have formed in an Iceland-like tectonic setting. MOR, mid-ocean ridge; cpx, clinopyroxene; ol, olivine; plag, plagioclase.

Received 24 September 2013; accepted 16 April 2014;
published online 25 May 2014

References

- Allen, R. M. *et al.* Plume-driven plumbing and crustal formation in Iceland. *J. Geophys. Res.* **107**, 1–19 (2002).
- Jakobsson, S. P., Jonasson, K. & Sigurdsson, I. A. The three igneous rocks series of Iceland. *Jökull* **58**, 117–138 (2008).
- Kroner, A. Evolution of the Archean continental crust. *Ann. Rev. Earth Planet. Sci.* **13**, 49–74 (1982).
- Carmichael, I. S. E. The petrology of Thingmuli, a tertiary volcano in eastern Iceland. *J. Petrol.* **5**, 435–460 (1964).
- Muehlenbachs, K., Anderson, A. T. & Sigvaldason, G. E. Low- O^{18} basalts from Iceland. *Geochim. Cosmochim. Acta* **38**, 577–588 (1974).
- Nicholson, H. *et al.* Geochemical and isotopic evidence for crustal assimilation beneath Krafla, Iceland. *J. Petrol.* **32**, 1005–1020 (1991).
- Bindeman, I. N. *et al.* Silicic magma petrogenesis in Iceland by remelting of hydrothermally altered crust based on oxygen isotope diversity and disequilibria between zircon and magma with implications for MORB. *Terra Nova* **24**, 227–232 (2012).
- Martin, E., Martin, H. & Sigmarsson, O. Could Iceland be a modern analogue for the Earth's early continental crust? *Terra Nova* **20**, 463–468 (2008).
- Harrison, T. M. The Hadean crust: Evidence from >4 Ga zircons. *Annu. Rev. Earth Planet. Sci.* **37**, 479–505 (2009).
- Condie, K. in *Earth's Oldest Rocks* Vol. 15 (eds Van Kranendonk, R., Smithies, H. & Bennett, V. C.) 9–18 (Developments in Precambrian Geology, 2007).
- Barker, F. & Arth, J. G. Generation of trondhjemitic-tonalitic liquids and Archean bimodal trondhjemite-basalt suites. *Geology* **4**, 596–600 (1976).
- Moyen, J. F. The composite Archean grey gneisses: Petrological significance, and evidence for a non-unique tectonic setting for Archean crustal growth. *Lithos* **123**, 21–36 (2011).
- Moyen, J. F. & Martin, H. Forty years of TTG research. *Lithos* **148**, 312–336 (2012).
- Martin, H. Effect of steeper Archean geothermal gradient on geochemistry of subduction-zone magmas. *Geology* **14**, 753–756 (1986).
- Rapp, R. P., Watson, E. B. & Miller, C. F. Partial melting of amphibolite/eclogite and the origin of Archean trondhjemites and tonalities. *Precamb. Res.* **51**, 1–25 (1991).
- Nair, R. & Chacko, T. Role of oceanic plateaus in initiation of subduction and origin of continental crust. *Geology* **36**, 583–586 (2008).
- Smithies, R. H., Champion, D. C. & Van Kranendonk, M. J. Formation of Paleoproterozoic continental crust through infracrustal melting of enriched basalt. *Earth Planet. Sci. Lett.* **281**, 298–306 (2009).
- Zegers, T. E. & van Keken, P. E. Middle Archean continent formation by crustal delamination. *Geology* **29**, 1083–1086 (2001).
- Bowring, S. A., Williams, I. S. & Compston, W. 3.96 Ga gneisses from the Slave province, Northwest Territories, Canada. *Geology* **17**, 971–975 (1989).
- Stern, R. A. & Bleeker, W. Age of the world's oldest rocks refined using Canada's SHRIMP: The Acasta Gneiss Complex, Northwest Territories, Canada. *Geosci. Can.* **25**, 27–31 (1998).
- Bowring, S. A. & Williams, I. S. Priscoan (4.00–4.03 Ga) orthogneisses from northwestern Canada. *Contrib. Min. Petrol.* **134**, 3–16 (1999).
- Iizuka, T. *et al.* Geology and zircon geochronology of the Acasta Gneiss Complex, northwestern Canada: New constraints on its tectonothermal history. *Precamb. Res.* **153**, 179–208 (2007).
- Iizuka, T. *et al.* 42 Ga zircon xenocryst in an Acasta gneiss from northwestern Canada: Evidence for early continental crust. *Geology* **34**, 245–248 (2006).
- Grove, T. L. & Kinzler, R. J. Petrogenesis of Andesites. *Ann. Rev. Earth Planet. Sci. Lett.* **14**, 417–454 (1986).
- Page, F. Z. *et al.* High-precision oxygen isotope analysis of picogram samples reveals 2 μm gradients and slow diffusion in zircon. *Am. Mineral.* **92**, 1772–1775 (2007).
- Valley, J. W. *et al.* Zircon megacrysts from kimberlite: Oxygen isotope variability among mantle melts. *Contrib. Min. Petrol.* **133**, 1–11 (1998).
- Taylor, H. P. & Sheppard, S. M. F. Igneous Rocks: I Processes of isotopic fractionation and isotope systematics. *Rev. Min. Geochem.* **16**, 227–271 (1986).
- Bindeman, I. N. & Valley, J. W. Low- $\delta^{18}\text{O}$ Rhyolites from Yellowstone: Magmatic evolution based on analyses of zircons and individual phenocrysts. *J. Petrol.* **42**, 1491–1517 (2001).

29. Trail, D., Watson, E. B. & Tailby, N. D. The oxidation state of Hadean magmas and the implications for the early Earth's atmosphere. *Nature* **480**, 79–83 (2011).
30. Balsley, S. D. & Gregory, R. T. Low-¹⁸O silicic magmas: Why are they so rare? *Earth Planet. Sci. Lett.* **162**, 123–136 (1998).

Acknowledgements

We thank R. Ickert and A. Burnham for advice on zircon strain partition modelling; J. Davies for critical discussions throughout; J. Ketchum and the Northwest Territories Geoscience Office staff for scientific and field support; and E. Thiessen for mapping assistance. We thank T. Iizuka and T. Kemp for constructive and informative reviews. This research was funded by National Science and Engineering Research Council of Canada grants to T.C. and L.M.H. as well as a Circumpolar/Boreal Alberta Research grant for fieldwork to J.R.R.

Author contributions

Mapping and sample collection was conducted by J.R.R. and T.C. Sample crushing, processing, and zircon separations were carried out by J.R.R., R.A.S. and J.R.R. carried out collection of zircon oxygen and U–Th–Pb isotopic data by SIMS. Chemical abrasion of zircon was carried out by J.R.R. and L.M.H. All authors contributed to discussion of results and their implications, as well as preparation of the manuscript.

Additional information

Supplementary information is available in the [online version of the paper](#). Reprints and permissions information is available online at www.nature.com/reprints. Correspondence and requests for materials should be addressed to J.R.R.

Competing financial interests

The authors declare no competing financial interests.

Earth's earliest evolved crust generated in an Iceland-like setting

Jesse R. Reimink, Thomas Chacko, Richard A. Stern, Larry M. Heaman

SIMS Analytical Methods

Three epoxy grain mounts (M1070, M1093, M1180) containing zircon from sample TC3 (CCIM sample number S1425) and various reference materials (RM) were prepared for SIMS analysis. Zircon RM for U-Pb calibration were TEM2 (S0022; 416.8 Myr³¹), 6266 (S0023; ²⁰⁶Pb/²³⁸U = 559.0 Myr³²), and OG1 (S0030; ²⁰⁷Pb/²⁰⁶Pb age = 3465.4 Myr; ²⁰⁶Pb/²³⁸U = 3441 ± 3 Myr³³) and for oxygen isotopes were TEM2 ($\delta^{18}\text{O}_{\text{V-SMOW}} = +8.2\text{‰}$ (31); $^{18}\text{O}/^{16}\text{O}_{\text{V-SMOW}} = 0.0020052$) and our lab zircon UAMT1 (S0081 = $\delta^{18}\text{O}_{\text{V-SMOW}} = +4.87\text{‰}$; R. Stern, unpublished data). Weighted mean and age calculations were carried out using Isoplot v. 3.76³⁴. Uranium decay constants are those of ref. [35].

M1070 and M1093 contained natural TC3 zircon, whereas M1180 contained TC3 zircon having been subjected to varying levels of annealing and chemical abrasion. The mounts were ground and polished with diamond compounds to expose zircon grain interiors, cleaned with alkaline soap, deionized water, and, in the case of U-Pb analyses, weak HCl. Surfaces were coated with 5 nm of Au for scanning electron microscopy (SEM), followed by an additional 20 nm prior to SIMS analysis. A Zeiss EVO MA15 SEM fitted with a broadband CL detector (ETP Semra, Pty. Ltd., Sydney, Australia) and semiconductor backscattered electron detector was employed for characterizing internal grain zonation. Typical beam conditions were 15 or 20 kV, and 3–5 nA.

Oxygen isotope (¹⁸O, ¹⁶O) compositions, which were measured prior to U-Pb isotopes, were determined from 156 spots on zircon TC3 in M1070 and M1093 in between March 2011 and March 2012 using the CCIM IMS 1280 ion microprobe. Instrument conditions and standardization are tabulated for each of the ion probe sessions in Table S8, and are summarized here. The ¹³³Cs⁺ primary beam conditions included an impact energy of 20 keV, ~15 μm diameter, and 3 nA current. A single analysis lasted 4.5 minutes and entailed rastering the probe for 30–45 s over a 20 × 20 μm area to clean and implant Cs, automated secondary ion tuning, and finally 100 s of isotopic measurements. The normal incidence electron gun was utilized for charge compensation. Negative secondary ions were extracted from the sample mount (–10 kV potential) into the secondary (transfer) column. Transfer conditions included a 120 μm entrance slit, a 5 mm wide rectangular field aperture, and 100× sample image magnification at the field aperture plane. The energy window utilized through 2011 was 50 eV, truncating high-energy ions, but subsequently no energy filtering was applied. The mass-separated oxygen isotopes were detected simultaneously in dual Faraday cups at the L'2 (¹⁶O[–]) and either H1 or H'2 (¹⁸O[–]) positions in the multi-detector array. Mass resolution ($\Delta m/M$ at 10% peak height) was typically

1900 and 2250, respectively. Secondary ion count rates for $^{16}\text{O}^-$ were $\sim 3 \times 10^9$ c/s. Faraday cup baselines were measured at the start of the day, and were sufficiently stable and low that no further measurements were necessary. Instrumental mass fractionation was monitored by analysis of TEM2 zircon once after every four unknowns, and data for the RM processed collectively for the analytical session lasting usually several hours. There was either no significant drift in the IMF during a session, or it was smoothly varying, in which case the data for unknowns were time-corrected back to the start of the session. Individual spot uncertainties at 95% confidence are typically $\pm 0.25\%$ (range: 0.14–0.37%), and include errors relating to within-spot counting statistics, between-spot (geometric) effects, and instrumental mass fractionation. Matrix effects relating to variations in zircon composition and structure (e.g., metamictization) are assumed to be negligible. The analytical results for the zircon RM S0081 run concurrently give an error-weighted mean for $\delta^{18}\text{O} = +4.87 \pm 0.033$ (n = 51; MSWD = 1.4; P = 0.039), and with two outliers rejected = $+4.87 \pm 0.031$ (MSWD = 1.12; P = 0.27), identical to the reference value. $\delta^{18}\text{O}_{\text{VSMOW}}$ was calculated as follows:

$$\delta^{18}\text{O}_{\text{VSMOW}} = ((^{18}\text{O}/^{16}\text{O}_{\text{SAMPLE}})/(^{18}\text{O}/^{16}\text{O}_{\text{VSMOW}}) - 1)$$

where $^{18}\text{O}/^{16}\text{O}_{\text{VSMOW}} = 0.0020052$, and reported in ‰.

SIMS analyses of U-Pb isotopes in TC3 zircon were carried out in six sessions, initially in December 2011, with most analyses occurring in January–February 2013. The methods varied slightly between sessions in experimenting with optimal analytical conditions. The primary beam characteristics included either $^{16}\text{O}^-$ (beam current = 4–11 nA) or $^{16}\text{O}_2^-$ (0.5–4 nA), impact energy = 23 keV, projected (Kohler) image mode, with probe (longest axis) diameter 10–25 μm . The primary beam was rastered around the analysis site for 2–3 minutes prior to data collection with a stationary primary beam. IMS1280 secondary ion extraction conditions included a sample image magnification of 200 \times at the field aperture, entrance slit width = 65–75 μm , and field aperture width = 4–6 mm. The energy slit was maintained fully open, except for one session (IP13010) where it was 75 eV and transmitting low energy ions. Positive secondary ions were collected sequentially with the axial electron multiplier and an exit slit width = 175 μm , giving a mass resolution (1% peak height definition) = 4500–4900.

Ten secondary ion mass positions (typical count times in seconds) were collected over five or six cycles: $^{196}\text{Zr}_2\text{O}^+$ (2), $^{204}\text{Pb}^+$ (20), $^{204.05}\text{background}^+$ (20), $^{206}\text{Pb}^+$ (10), $^{207}\text{Pb}^+$ (20), $^{208}\text{Pb}^+$ (3), $^{238}\text{U}^+$ (3), $^{248}\text{ThO}^+$ (3), $^{254}\text{UO}^+$ (3), and $^{270}\text{UO}_2^+$ (5). Data were processed using SQUID2 software³⁶, in a custom version designed for processing data output from the IMS 1280. The $^{206}\text{Pb}/^{238}\text{U}$ ages were calibrated against TEM2 zircon, using a calibration constant ('a') determined from the relationship $^{206}\text{Pb}^+/^{270}\text{UO}_2^+ = a \times (^{270}\text{UO}_2^+/^{254}\text{UO}^+)^m$, where the m ranged from 0.2 to 0.8 (average 0.5) for TEM2 data. Spot-to-spot excess uncertainties in the $^{206}\text{Pb}/^{238}\text{U}$ values (not accounted for by within-spot counting uncertainties) determined from analyses of

TEM2 ranged from $\pm 0\%$ to 1.1% (68% confidence), and a minimum of $\pm 0.5\%$ was propagated to the unknowns (see ref. [32]). Uranium abundances were calibrated against 6266 zircon with $U = 903$ ppm, utilizing $^{270}\text{UO}_2^+ / ^{196}\text{Zr}_2\text{O}^+$. The Th/U ratios and Th abundances were determined from $^{248}\text{ThO}^+ / ^{254}\text{UO}^+$ using measured $^{232}\text{Th} / ^{238}\text{U}$ discrimination factors for the session (~ 1.0).

The radiogenic Pb-isotopes were corrected for common Pb using ^{204}Pb , assuming a model crustal composition³⁷ at the $^{206}\text{Pb} / ^{238}\text{U}$ age of the sample. All count rates were corrected for deadtime = 44 ns. The mean $^{206}\text{Pb} / ^{238}\text{U}$ age determined for 6266 zircon ($n = 28$) analyzed concurrently is 564 ± 2.9 (MSWD = 5.2), a value that is marginally but statistically higher than the reference age of 559 Myr. The mean $^{206}\text{Pb} / ^{238}\text{U}$ age determined for OG1 zircon ($n = 50$, minus 3 outliers) is 3436 ± 5 Myr (MSWD = 1.05), which is within uncertainty of the reference value of 3441 Myr. The data for the secondary RM's suggest that inaccuracies in the $^{206}\text{Pb} / ^{238}\text{U}$ ages for the unknowns will be $< \pm 1.0\%$. The mean $^{207}\text{Pb} / ^{206}\text{Pb}$ age calculated for secondary RM OG1 zircon ($n = 50$) is 3463.6 ± 1.3 (MSWD = 1.5), and allowing for six rejects (high and low), is 3463.8 ± 1.0 (MSWD = 0.72). These mean values are slightly but statistically lower than the reference value of 3465.4 Myr, suggesting that the $^{207}\text{Pb} / ^{206}\text{Pb}$ ratios for the unknowns are also likely to be biased slightly low. In this study, the $^{207}\text{Pb} / ^{206}\text{Pb}$ ratios were not corrected for this bias, which is probably due to instrumental mass fractionation, with a mean IMF for $^{207}\text{Pb} / ^{206}\text{Pb}$ of -0.97% ³³, equivalent to -1.5 Myr at 4000 Myr.

Zircon trace-element analyses were obtained using the Cameca IMS 4f Ion Microprobe at the Edinburgh Ion Microprobe Facility, University of Edinburgh following the procedures of ref. [38]. Uncertainties in the trace-element analyses are dependent on the concentration of the elements measured. Typical uncertainties for elements with concentrations > 100 ppm are $\leq 1\%$ while for elements with concentration between 1-10 ppm uncertainties are $\leq 10\%$. Low concentrations, which are typically less than 0.1 ppm, may have uncertainties $\geq 50\%$.

Whole-Rock Analytical Methods:

Samples were collected during 2010 and 2011 field seasons in the Acasta river area, Northwest Territories, Canada. In order to conduct whole-rock geochemical analyses and zircon mineral separation, between 0.5–2 kg of rock from each sample was pulverized using a shatterbox. Whole-rock major-, minor-, and trace-element geochemistry by XRF³⁹ and ICP-MS⁴⁰ was conducted at the Washington State University's GeoAnalytical Laboratory.

Map:

Figure S1 locates the Acasta Gneiss Complex (AGC) on the western margin of the Slave Craton, Northwest Territories, Canada. Figure S2 provides a simplified geologic map of the area surrounding the Idiwhaa Tonalitic Gneiss. The rocks in the mapped area are generally less

strained than those in many other parts of the AGC, particularly the highly strained western portion²¹⁻²². We have identified 5 major rock units in this simplified map. The five rock units (see Fig. S3 for field photos) are as follows; 1) the Idiwhaa Tonalitic Gneiss 2) banded biotite tonalitic gneiss interlayered at a decimeter scale, but differentiated from the Idiwhaa Tonalitic Gneiss by lack of combined garnet and amphibole and overall more felsic compositions; 3) a coarse-grained metagabbro dominated by plagioclase and amphibole (after pyroxene) and lacking significant fabric; 4) amphibolite gneisses commonly associated with the banded tonalitic gneisses and cross-cut by leucocratic veinlets; 5) foliated biotite granodiorite and granite that intrude units 1-4. A single mafic dike, likely of Paleoproterozoic age, cross-cuts all the units and is discontinuously traceable across the map area.

The Idiwhaa Tonalitic Gneiss extends for at least 5 x 40 meters (see Table S5 for GPS coordinates), trending ~210°, parallel to the local foliation. At the outcrop scale, the unit is variably intruded by cm-scale white leucocratic veinlets with foliation defined by biotite and amphibole trending roughly parallel to the unit strike. Bounded on both sides by banded biotite tonalitic gneiss, the ITG is a garnet-biotite-hornblende tonalitic gneiss. Modal abundance determinations on one sample (TC3) yielded the following mineral proportions: plagioclase (32%), quartz (23%), hornblende (20%), biotite (19%), Fe-Ti oxides (4%), and garnet (1.4%), along with accessory K-feldspar, apatite, titanite, and zircon.

Zircon U-Pb Systematics

Zircons were extracted from one pulverized sample of Idiwhaa Tonalitic Gneiss (sample TC3, CCIM internal sample S1425) by standard magnetic and heavy liquid mineral separation techniques. A subset of these zircons was selected based on clarity and lack of inclusions and subsequently mounted in epoxy resin for later CL imaging and analysis by SIMS.

Zircons from sample TC3 can collectively be subdivided into four distinct morphological or textural phases (see zircon phases I–IV in Fig. 2A). These zircon phases are strikingly similar to those described by previous workers from other ca. 4.0 Gyr AGC rocks²¹. Phase I zircon comprises less CL-responsive grain centers of various sizes with generally well-formed crystal boundaries. These are overgrown by Phase II zircon, a chemically distinct CL responsive growth zone characterized by fine-scale oscillatory zoning. Phases I and II are both interpreted to be of magmatic origin (Fig. 2A). Phase III zircon consists of dark-CL areas, generally occurring as cross-cutting embayments and irregular incursions into Phase I and II zones (Fig. 2B). Phases I–III are overgrown by Phase IV zircon, which consists of thin (5–30 μm wide) overgrowths (Fig. 2B) exhibiting no zoning, which we interpret to be of metamorphic origin.

We obtained a total of 160 U-Pb isotope analyses from 68 zircon grains extracted from sample TC3 (Fig. S5). The ages of Phase I and II zircon are indistinguishable within analytical

uncertainty; both record $^{207}\text{Pb}/^{206}\text{Pb}$ ages ranging from 4030 to 3840 Myr (Table S2; Fig. S6) with variable degrees of discordance. Phase I zircon records $^{207}\text{Pb}/^{206}\text{Pb}$ dates between 3849 and 4041 Myr and discordance between -1.5 and 3% . Phase II zones record a similar span in $^{207}\text{Pb}/^{206}\text{Pb}$ ages (3844–4033 Myr) but with more variable discordance (-1.3% to 6.7% ; Fig. S5). Approximately half of the Phase II analyses with discordance $> 1\%$ record $^{207}\text{Pb}/^{206}\text{Pb}$ ages > 4000 Myr, suggesting that recent Pb-loss has occurred within these grains. Both igneous phases of zircon growth show signs of recent and ancient Pb-loss (Fig. S7).

It is important to note that nearly all of the analyses ($n = 121$) of Phase I and II magmatic zircon plot near the upper end of a broad discordia array with an upper intercept exceeding 4.0 Gyr (Fig. S5). This observation strongly suggests that Phase I and II comprise a single population of magmatic zircon that records the crystallization age of the magmatic protolith of Idiwhaa Tonalitic Gneiss.

Analyses from Phase III areas are discordant and generally fall toward the lower end of a discordia array with an upper intercept of > 4.0 Gyr and lower intercept of ~ 3.2 Gyr. Phase IV overgrowths yielded a wider range of $^{207}\text{Pb}/^{206}\text{Pb}$ ages between 3.75 and 3.17 Gyr and typically have low Th/U (< 0.3 in Table S2). The most concordant of these data cluster at ~ 3.2 Gyr, which we interpret to represent the approximate time of metamorphic zircon growth. Phase IV analyses with older $^{207}\text{Pb}/^{206}\text{Pb}$ ages may reflect incorporation of some proportion of older zircon phases (I–III) in the analyses due to the small size of the Phase IV overgrowths. Younger, discordant ages from Phase IV areas likely reflect ~ 3.2 Gyr metamorphic zircon that has undergone more recent Pb-loss.

The reason for the spread in $^{207}\text{Pb}/^{206}\text{Pb}$ ages of Phase I and II zircon between ~ 4030 and ~ 3940 Myr is unclear. This age dispersion along concordia has also been documented in previous studies of ancient AGC samples^{19–22} and may reflect Pb-loss during a younger (ca. ~ 3200 Myr) metamorphic event, or an even earlier (ca. ~ 3900 – 3950 Myr) disturbance.

In order to better understand the nature of this shallow ‘smearing’ of ages along concordia, we performed chemical abrasion⁴² on aliquots of TC3 zircon, before subsequent analysis by SIMS. Grains were annealed at 1000 °C for up to 48 hours followed by etching with solution of HF and H_2O (50:50) for up to 28 hours. The probability of obtaining > 4.0 Gyr $^{207}\text{Pb}/^{206}\text{Pb}$ ages is higher in TC3 zircons that have undergone chemical abrasion. Although some of this increase may be due to removal of domains where Pb-loss was significant, we suggest that the main effect of chemical abrasion was to highlight radiation damaged regions within the zircons so that they could be avoided in SIMS analysis.

Ninety-two analyses of Phase I and II zircon yield $^{207}\text{Pb}/^{206}\text{Pb}$ dates ≥ 3980 Myr. The results of a three-component unmixing treatment⁴³ of these data indicate a dominant age peak (51% of the analyses) of 4013.3 ± 1.0 Myr. A similar weighted mean $^{207}\text{Pb}/^{206}\text{Pb}$ date of $4014.6 \pm$

1.1 Myr (MSWD = 0.96) is obtained based on the 40 oldest zircon analyses. Due to the slight bias in the SIMS $^{207}\text{Pb}/^{206}\text{Pb}$ ages (see above), these results should be corrected by +1.5 Ma, i.e. 4014.8 ± 1.1 Myr and 4016.1 ± 1.1 Myr, respectively. We interpret these calculations to give a minimum estimate for the crystallization age of the igneous protolith of the ITG.

A regression of 34 Phase I and II zircon analyses of zircon that had been treated by chemical abrasion yields an upper intercept age of 4026 ± 18 Myr (MSWD = 2.2), which is in agreement with the age estimate noted above. Based on the similarity of ages for the oldest zircon analyses calculated in various ways and the large number of concordant or near concordant ($\leq 2\%$ discordant) analyses with $^{207}\text{Pb}/^{206}\text{Pb}$ ages between 4032 and 4015 Myr ($n = 18$) within this population, our preferred estimate for the time of igneous zircon crystallization (both Phase I and Phase II growth zones) is 4.02 Gyr. We conclude that the Idiwhaa unit represents a single-phase tonalite with a coherent zircon U-Pb dataset. These igneous growth phases were subsequently overprinted by one or more metamorphic recrystallization events, the most recent occurred at ~ 3.2 Gyr.

Zircon Trace-Element Systematics

A suite of trace-elements were analyzed for at the Edinburgh Ion Microprobe Facility³⁸ from each of the four different phases of zircon identified in sample TC3 of the ITG. These data are presented in Table S4 along with other data (U-Th-Pb and O-isotope) that correlates to the same spot or growth zone from which the trace-element data were obtained.

REE abundances and patterns vary significantly with zircon growth phase. Phase I and II magmatic zircon domains have broadly similar REE patterns typical of igneous zircons, including highly enriched HREE (relative to LREE) and significant positive Ce and negative Eu anomalies (Fig. S8A). Phase III and IV metamorphic zircon display REE patterns much more enriched in the LREE, typical of metamorphic and hydrothermal zircons⁴⁴.

We focus specifically on the REE patterns recorded in Phase I and II igneous zircon. Notably, the REE content of the radiation-damaged parts of igneous zircon can be affected by fluid alteration. Calcium is commonly used as an indicator of the degree of fluid alteration as it tends to be enriched in metamict zones⁴⁵. We have therefore filtered out Phase I and II analyses with >4 ppm Ca, as analyses with higher Ca contents have variably enriched LREE contents (Fig. S8B). After filtering, the Phase I and II analyses produce a coherent data set for both growth phases of TC3 zircon inferred to be of igneous origin (Fig. S8A)

Though the two igneous phases of TC3 zircon have similar shaped REE patterns, they differ in their overall abundance of REEs, except the Ce content. This similarity in Ce content may be viewed as an increase in degree of Ce anomaly. Specifically, Phase II zircon has a larger

positive Ce anomaly than Phase I, which, given the greater affinity of zircon for Ce^{4+} relative to Ce^{3+} , requires that Phase II zircon has a higher $\text{Ce}^{4+}/\text{Ce}^{3+}$.

Figure S9 shows the relationships between the magnitude of the Ce anomaly (Ce/Ce^*), zircon crystallization temperature, and oxygen fugacity as calibrated by ref. [29]. The temperature of zircon crystallization is inferred from Ti-in-zircon geothermometry⁴⁶ and the oxygen fugacity is referenced to several common oxygen fugacity buffer equilibria. Overall, this plot shows that, at comparable Ti-in-zircon temperatures, Phase II zircon crystallized from a more oxidized magma (i.e., has a larger Ce anomaly) than Phase I zircon. We suggest that this oxidation of the magma occurred due to assimilation of rocks previously altered by surface waters. Even under the reducing atmospheric conditions of the early Earth (i.e., O_2 at $\sim 10^{-13}$ present atmospheric levels)⁴⁷⁻⁴⁸, surface-water alteration would have caused rocks to become more oxidized than their unaltered, mantle-derived precursors.

Validity of Whole-Rock REE Patterns

Although REEs are considered to be relatively immobile during metamorphism, the ability of whole-rocks to preserve primary igneous REE signatures in ancient, poly-metamorphic terranes such as the AGC must be evaluated. An initial check on the robustness of the Idiwhaa whole-rock REE data may be done by comparing the pattern of measured zircon/whole-rock REE ratios with those predicted by lattice strain theory⁴⁹⁻⁵⁰. In particular, if the REE systematics of the whole-rock have not been disturbed by metamorphism, and if the zircon in question was part of the crystallizing magmatic assemblage, then REE data plotted on a so-called Onuma diagram should be well fit by an equation of the form:

$$D_i = D_o \times \exp \left\{ \frac{-4\pi EN_A \left[\frac{r_o}{2}(r_i - r_o)^2 + \frac{1}{3}(r_i - r_o)^3 \right]}{RT} \right\}$$

where E is the Young's Modulus of the REE-bearing site (in GPa), and D_i is the partition coefficient for an ion of radius r_i (in Å) within a specific structural site. D_o is then the theoretical partition coefficient for an ion with ideal radius r_o . Finally, N_A is Avagadro's number, R is the gas constant, and T is the temperature in K⁵⁰. As shown in Figure S10, the data for both Phase I and II zircon show a good parabolic fit to the lattice strain equation as is typical for zircon hosted in the magmatic rock in which it crystallized⁵¹. In contrast, average metamorphic zircon is not well fit by the lattice strain equation (Fig. S10). It should be noted that three elements were excluded from the fitting procedure for both the Phase I and II data: Ce and Eu were not included because of their divergence from theoretical partitioning due to variable valence states; La was excluded from all fits because its very low concentration in zircon leads to large relative uncertainties in

the measured values in zircon. General conclusions that may be drawn from this analysis are the whole-rock REE systematics of the Idiwhaa unit and Phase I and II zircon REE patterns are broadly in equilibrium, indicating that ITG whole-rock REE compositions have not been greatly modified by post-magmatic processes.

A second test of the robustness of the REE systematics within the ITG is to compare the measured whole-rock REE pattern for tonalite sample TC3 with a theoretical REE pattern calculated to be in equilibrium with Phase I and II zircon. We undertook two different sets of calculations: first, we employed the widely used zircon/ground-mass partition coefficients of ref. [52] derived from a felsic volcanic rock (~73 wt.% SiO₂); and secondly, we used zircon/whole-rock partition coefficients deduced from diorite (BP39) and mafic granodiorite (BP7) samples from the well characterized Boggy Plain pluton of Australia⁵³⁻⁵⁴, which contain ~52 and 61 wt.% SiO₂, respectively. Melt composition can have a significant effect on mineral/melt or whole-rock partition coefficients and thus the partition coefficients deduced from the Boggy Plain samples may be more appropriate than the ref. [52] partition coefficients for Idiwhaa tonalite sample TC3 investigated in the present study, which contains ~58 wt.% SiO₂.

Though the whole-rock REE abundances deduced from Phase II zircon are distinctly lower than measured whole-rock abundances, both sets of calculated REE patterns provide a reasonably good match to the overall shape of the measured pattern (Fig. S11). Specifically, both calculated and measured patterns show a negative Eu anomaly and relatively little LREE to HREE fractionation when the patterns are calculated using the Boggy Plain partition coefficients. Importantly, none of the calculated patterns resemble the steep REE patterns of later Archean TTGs¹²⁻¹⁴.

The difference in whole-rock REE contents calculated from Phase I and II zircon requires some evaluation (Fig. S11). One possible explanation for this difference is that the crystallization of another REE-rich accessory mineral occurred after the crystallization of Phase I zircon but before the crystallization of Phase II. In particular, the crystallization of titanite, which has an overall affinity for REE but does not strongly fractionate LREE from HREE⁵⁵, could cause an overall decrease in melt REE content without greatly affecting the overall shape of the melt REE pattern. It then follows that late-crystallizing Phase II zircon would inherit these lower REE contents, yet still exhibit the same basic REE profile as Phase I zircon. Our proposed model of magma evolution through combined assimilation-fractional crystallization (AFC) processes is consistent with such a scenario.

On the basis of these zircon trace-element analyses, we conclude that the measured whole-rock REE composition of this ancient Acasta gneiss sample provides a good approximation of the REE composition of the igneous protolith of the sample. Thus, petrogenetic

inferences drawn from these whole-rock REE data should provide robust constraints on the origin and formation of the earliest known continental crust on Earth.

Zircon Oxygen-Isotope Systematics

Because of the slow diffusion rates of oxygen in zircon, this mineral has the capacity to retain a record of primary, igneous oxygen isotopic signatures, even through high-grade metamorphic events. This fact is evidenced by the preservation of sharp oxygen isotope gradients between igneous cores and metamorphic overgrowths in zircon grains that have undergone granulite-facies metamorphism⁵⁶. This same feature is seen in the zircons of Idiwhaa tonalite sample TC3, where the $\delta^{18}\text{O}$ values of metamorphic zircon growth Phases III and IV are markedly different than those of immediately adjacent Phase II igneous zircon. From this we conclude that zircon Phases I and II retain their original magmatic oxygen isotope compositions, which may therefore be used to make inferences about the igneous history of the Idiwhaa unit.

We analyzed oxygen isotopes from a total of 156 spots from 78 zircon grains extracted from ITG sample TC3. A subset of these grains was also analyzed for their U-Pb isotopic and trace-element compositions. The entire zircon oxygen isotope data set for Idiwhaa sample TC3 is summarized in Figure S12 and Table S3.

The main finding of this oxygen isotope study is a $\sim 0.8\%$ decrease in $\delta^{18}\text{O}$ values between Phase I and II zircon growth zones. We argued previously that this decrease must be linked to changes in the oxygen isotope composition of the magma throughout zircon crystallization, which in turn, most likely resulted from assimilation of surface-water altered, low- $\delta^{18}\text{O}$ crustal material. Other potential explanations for the observed shift in $\delta^{18}\text{O}$ values from one igneous zircon growth domain to the next cannot adequately explain the direction or magnitude of the observed shift. For example, several workers have noted that differences in the Hf content of zircons can have a small but detectable effect on the instrumental mass fractionation factor (IMF) used to correct oxygen isotope ratios measured by SIMS⁵⁶⁻⁵⁷. Thus, in principle, the apparent differences in the $\delta^{18}\text{O}$ values of Phase I and II zircon could be an artifact of differences in their Hf contents. In this case, however, the Hf contents of Phase I and II zircon are nearly identical (~ 0.85 wt.% Hf) and thus cannot be the cause of the observed differences in their $\delta^{18}\text{O}$ values. Another explanation may be closed-system fractional crystallization, which can also cause a shift in magmatic $\delta^{18}\text{O}$ values, however, in this case the effect is usually small, and when it occurs, generally results in a small increase in $\delta^{18}\text{O}$ values of the residual magma⁵⁸, rather than a decrease.

Additionally, it has been shown that radiation-damaged zircon material will preferentially react with fluids and could exchange enough oxygen to alter the measured oxygen isotopic ratios. Phase II zircon material is slightly more discordant than Phase I material (see the zircon

U-Pb discussion above), potentially suggesting that these areas may be more likely to have non-magmatic oxygen isotope ratios. However, Figure S13 indicates that Phase I material has higher concentrations of U+Th, indicating these areas would be more likely to accumulate radiation damage than Phase I. This corroborates with the textual evidence in which Phase I zircon is preferentially recrystallized by later metamorphic events. This may explain the higher scatter in the Phase I oxygen isotopic dataset (Fig. 2C). Additionally, though Phase II zircon is more discordant, the measured $\delta^{18}\text{O}$ values are consistent and not correlated with discordancy, indicating that no resetting of Phase II zircon oxygen isotopic ratios has occurred. We therefore conclude that the documented decrease in $\delta^{18}\text{O}$ values between Phase I and Phase II zircon growth in the ITG reflects assimilation of low $\delta^{18}\text{O}$ crustal material by the Idiwhaa magma.

Intra-grain variations in $\delta^{18}\text{O}$ values of igneous zircons have been documented in a number of Phanerozoic volcanic centers^{8,28,59}. These variations, along with phenocryst-melt disequilibrium from places such as Yellowstone, Iceland, and Kamchatka, are attributed to long phenocryst residence times in pre-eruptive magma chambers with varying oxygen isotopic compositions. Ref. [8] documented Icelandic zircons with heterogeneous $\delta^{18}\text{O}$ characterized by mantle-like $\delta^{18}\text{O}$ values in cores overgrown by igneous rims with values down to 1.5‰. These variations were attributed to assimilation or partial melting of low $\delta^{18}\text{O}$ crustal material, whereas zircon material with mantle-like $\delta^{18}\text{O}$ simply did not re-equilibrate with changing magma oxygen isotope composition. Ref. [28] attributed a core to rim decrease in $\delta^{18}\text{O}$ values of several per mil to a model of ‘crustal cannibalism’, whereby a magma chamber’s heat flux into overlying rocks hydrothermally alters these rocks followed by caldera collapse and assimilation of low $\delta^{18}\text{O}$ material. Due to the similarity of U-Pb ages between the two igneous phases of zircon growth documented here for the ITG, we also interpret the corresponding shift in oxygen isotope values to reflect a significant (~0.8‰) change in magma oxygen isotopic composition during zircon crystallization, ultimately caused by a similar process of ‘crustal cannibalism’ at ~4.02 Gyr. Interestingly, ref. [60] also invoked ‘crustal cannibalism’ to explain low $\delta^{18}\text{O}$ zircons from an early Archean gneiss terrane in West Greenland.

Supplementary References:

31. Black, L. P., Kamo, S. L., Allen, C. M., Davis, D., Aleinikoff, J. N., Valley, J. W., Mundil, R., Campbell, I. H., Korsch, R. J., Williams, I. S., and Foudoulis, C., Improved $^{206}\text{Pb}/^{238}\text{U}$ microprobe geochronology by the monitoring of a trace-element-related matrix effect; SHRIMP, ID-TIMS, ELA-ICP-MS and oxygen isotope documentation for a series of zircon standards. *Chem. Geol.* **205**, 115–140. (2004).
32. Stern, R. A. and Amelin, Y., Assessment of errors in SIMS zircon U-Pb geochronology using a natural zircon standard and NIST SRM 610 glass. *Chem. Geol.* **197**, 111–146. (2003).
33. Stern, R. A., Bodorkos, S., Kamo, S. L., Hickman, A. H., and Corfu, F., Measurement of SIMS instrumental mass fractionation of Pb isotopes during zircon dating. *Geostandards and Geoanalytical Research* **33**, 145–168 (2009).
34. Ludwig, K. R., Isoplot 3.75: A Geochronological Toolkit for Microsoft Excel. *Berkeley Geochronology Center Special Publication* **5**, 75 (2012), (http://www.bgc.org/isoplot_etc/isoplot/Isoplot3_75-4_15manual.pdf).
35. Jaffey, A. H., Flynn, K. F., Glendenin, L. E., Bentley, W. C., and Essling, A. M., Precision measurement of half-lives and specific activities of ^{235}U and ^{238}U . *Physical Review C: Nuclear Physics* **4**, 1889–1906. (1971).
36. Ludwig, K. R. SQUID2: A User's Manual, rev. 12 Apr, *Berkeley Geochronology Center Special Publication* **5**, 110 p. (2009), (http://www.bgc.org/isoplot_etc/squid/SQUID2_5Manual.pdf).
37. Stacey, J. S. and Kramers, J. D., Approximation of terrestrial lead isotope evolution by a two-stage model. *Earth Planet. Sci. Lett.* **26**, 207–221. (1975).
38. Hinton, R.W. & Upton, B.G.J. The chemistry of zircon: Variations within and between large crystals from syenite and alkali basalt xenoliths. *Geochim Cosmochim Acta* **55**, 3287-3302 (1991)
39. Johnson, D.M. Hooper, P.R. & Conrey, R.M. XRF Analysis of Rocks and Minerals for Major and Trace Elements on a Single Low Dilution Li-tetraborate Fused Bead. *Inter. Centre Diff. Data* 843-867 (1999)
40. Knaack, C.S. Cornelius, S. & Hooper, P.R. Trace element analyses of rocks and minerals by ICP-MS. Open-file report, Department of Geology, Washington State University, Pullman (1994)
41. Nui, Y. & O'Hara, M.J. Origin of ocean island basalts: A new perspective from petrology, geochemistry, and mineral physics considerations. *J. Geophys. Res.* **108**, 1–19 (2003).
42. Mattinson, J.M. Zircon U-Pb chemical abrasion (“CA-TIMS”) method: Combined annealing and multi-step partial dissolution analysis for improved precision and accuracy of zircon ages. *Chem. Geol.* **220**, 47–66 (2005).
43. Sambridge, M., Compston, W., Mixture modeling of multi-component data sets with application to ion-probe zircon ages. *Earth Planet. Sci. Lett.*, **128**, 373-390. (1994)

44. Hoskin, P.W.O. & Schaltegger, U. The Composition of Zircon and Igneous and Metamorphic Petrogenesis. *Rev. Min.* **53**, 27–62 (2003).
45. Geisler, T. *et al.* Transport of uranium, thorium, and lead in metamict zircon under low-temperature hydrothermal conditions. *Chem. Geol.* **191**, 141–154 (2002).
46. Ferry, J.M. & Watson, E.B. New thermodynamic models and revised calibrations for the Ti-in-zircon and Zr-in-rutile thermometers. *Contrib. Mineral. Petrol.* **154**, 429–437 (2007).
47. Kastin, J.F. Earth's Early Atmosphere. *Science* **259**, 920–926 (1993).
48. Catling, D.C. & Claire, M.W. How Earth's atmosphere evolved to an oxic state: A status report. *Earth Planet. Sci. Lett.* **237**, 1–20 (2005).
49. Onuma, N. *et al.* Trace element partitioning between two pyroxenes and the host lava. *Earth Planet. Sci. Lett.* **5**, 47–51 (1968).
50. Blundy, J. & Wood, B. Prediction of crystal-melt partition coefficient from elastic moduli. *Nature* **372**, 452–454 (1994).
51. Hanchar, J.M. & van Westrenen, W. Rare Earth Element Behavior in Zircon-Melt Systems. *Elements* **3**, 37–42 (2007).
52. Sano, Y. Terada, K. & Fukuoka, T. High mass resolution ion microprobe analysis of rare earth elements in silicate glass, apatite and zircon: lack of matrix dependency. *Chem. Geol.* **184**, 217–230 (2002).
53. Hoskin, P.W.O. Patterns of chaos: Fractal statistics and the oscillatory chemistry of zircon. *Geochim. Cosmochim. Acta* **64**, 1905–1923 (2000).
54. Hoskin P.W.O. *et al.* Identifying Accessory Mineral Saturation during Differentiation in Granitoid Magmas: an Integrated Approach. *J. Petrol.* **41**, 1365–1396 (2000).
55. Prowatke, S. & Klemme, S. Effect of melt composition on the partitioning of trace elements between titanite and silicate melt. *Geochim. Cosmochim. Acta* **69**, 695–709 (2005).
56. Peck, W.H. Valley, J.W. & Graham, C.M. Slow oxygen diffusion rates in igneous zircons from metamorphic rocks. *Am. Mineral.* **88**, 1003–1014 (2003).
57. Valley, J.W. Oxygen Isotopes in Zircon. *Rev. Min.* **53**, 343–385 (2003).
58. Eiler, J.M. Oxygen Isotope Variations of Basaltic Lavas and Upper Mantle Rocks. *Rev. Min.* **43**, 319–364 (2001).
59. Bindeman, I. Oxygen Isotopes in Mantle and Crustal Magmas as Revealed by Single Crystal Analysis. *Rev. Min.* **69**, 445–478 (2008).
60. Hiess, J. *et al.* Archaean fluid-assisted crustal cannibalism recorded by low $\delta^{18}\text{O}$ and negative $\epsilon_{\text{Hf(T)}}$ isotopic signatures of West Greenland granite zircon. *Contrib. Min. Petrol.* **161**, 1027–1050 (2011)
61. St. Onge, M.R. King, J.E. & Lalonde, A.E. Geology, east-central Wopmay Orogen, District of Mackenzie, Northwest Territories. *Geological Survey of Canada Open-File Report* **1923**, 3 sheets (1988)

62. Bleeker, W. & Davis, W.J. The 1991-1996 NATMAP Slave Province Project: Introduction. *Can. J. Earth Sci.* **36**, 1033-1042 (1999)
63. McDonough, W.F. & Sun, S.s. The composition of the Earth. *Chemical Geology* **120**, 223–253 (1995)

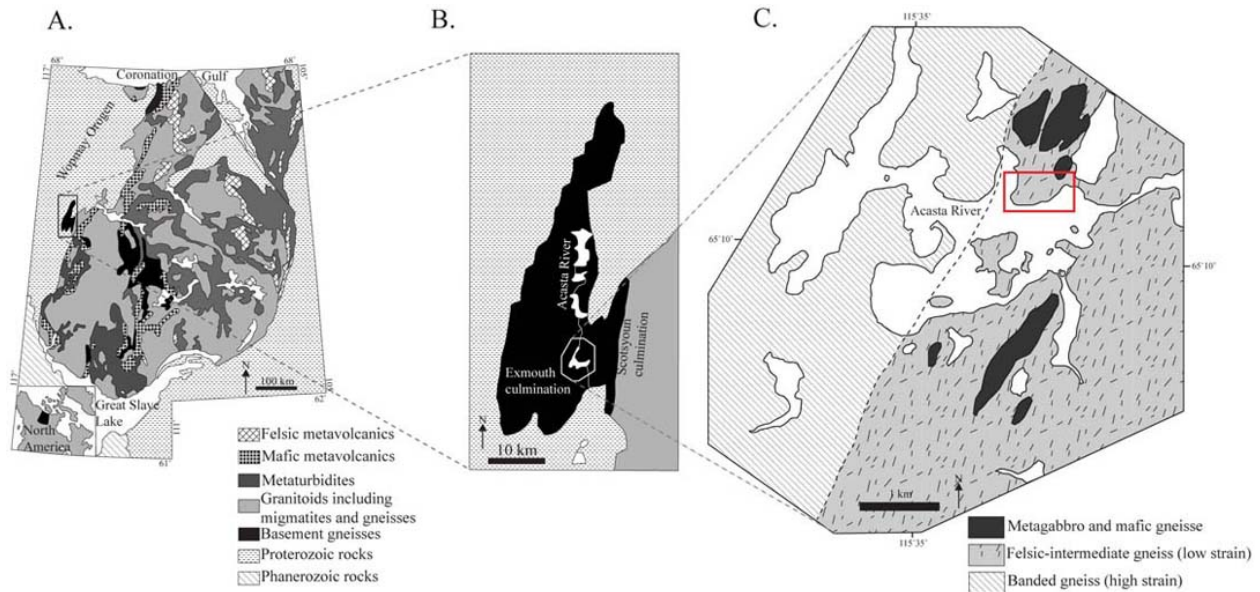


Fig. S1: Simplified geologic map: (A) The simplified geology of the Slave craton showing location of the Acasta Gneiss Complex on its western margin (B) modified after⁶¹⁻⁶². (C): Simplified lithologic map of the area immediately surrounding the mapped study area, modified from²². Extent of detailed mapping of the peninsula containing the 4.02 Gyr Idiwhaa Tonalitic Gneiss is shown in red.

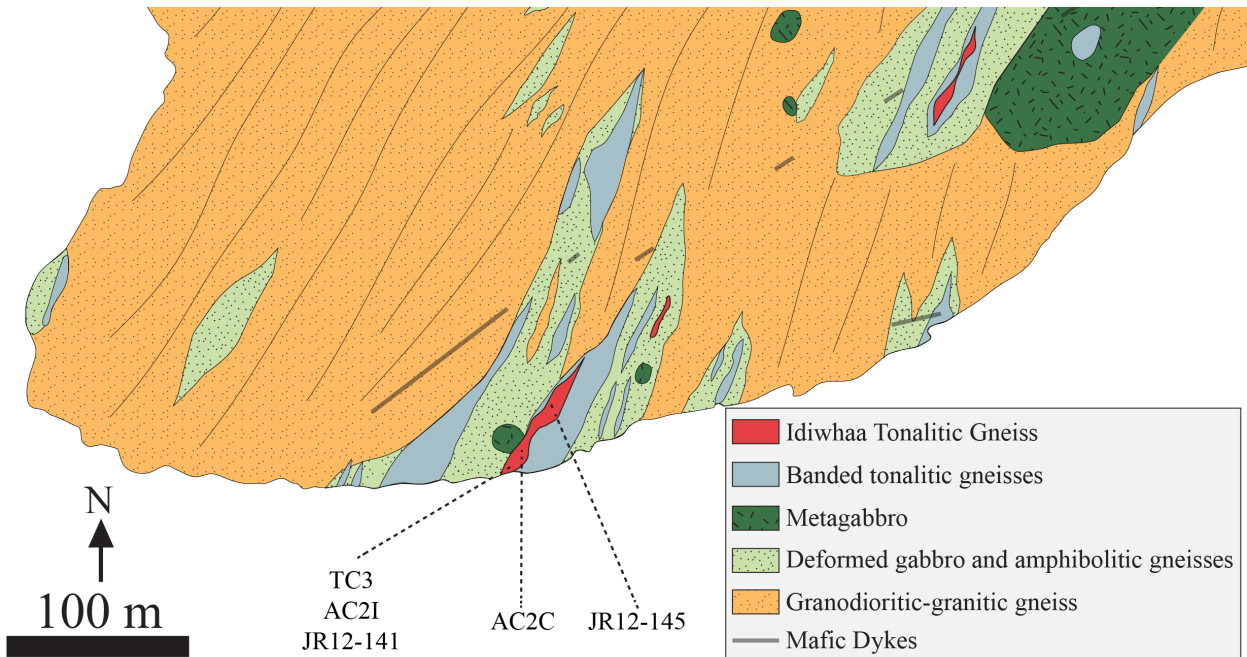


Fig. S2: Detailed geologic map of the region where the Idiwhaa Tonalitic Gneiss is exposed. Units in the legend are described in the text. Most contacts are inferred. Locations of samples discussed in the study are shown on the map.

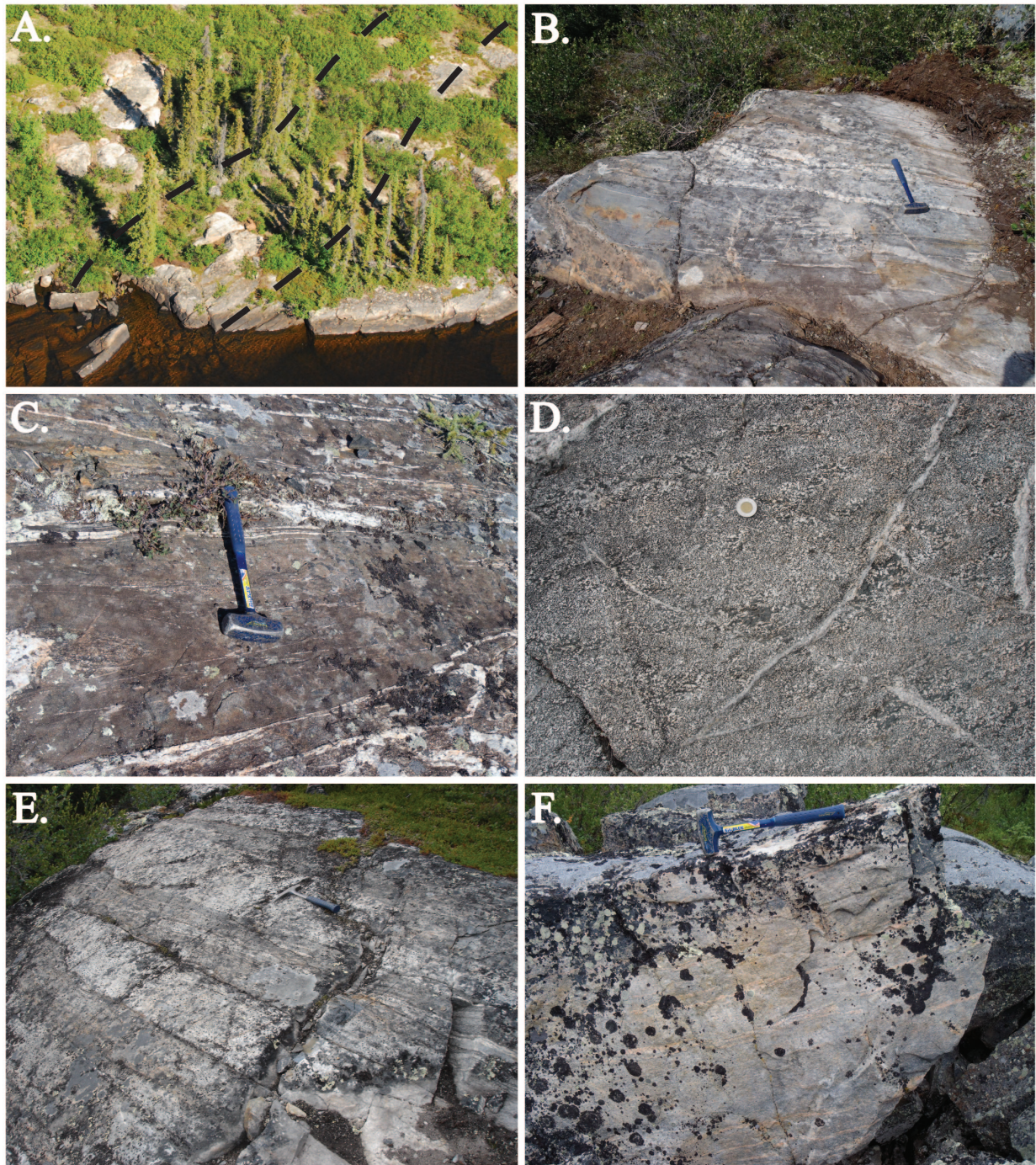


Fig. S3: Outcrop photos of rock units mapped within the low-strain study area. A: Aerial photo of the portion of the mapped peninsula containing the TC3 sample locality. The boundaries for the Idiwhaa Tonalitic Gneiss are roughly outlined. B: Outcrop photo of the TC3 sample locality. C: Photo of the deformed amphibolitic gneiss. D: Outcrop of coarse-grained metagabbro. E: Example of the banded biotite tonalitic gneiss interlayered at a decimeter scale. F: Outcrop of foliated granitic gneiss.

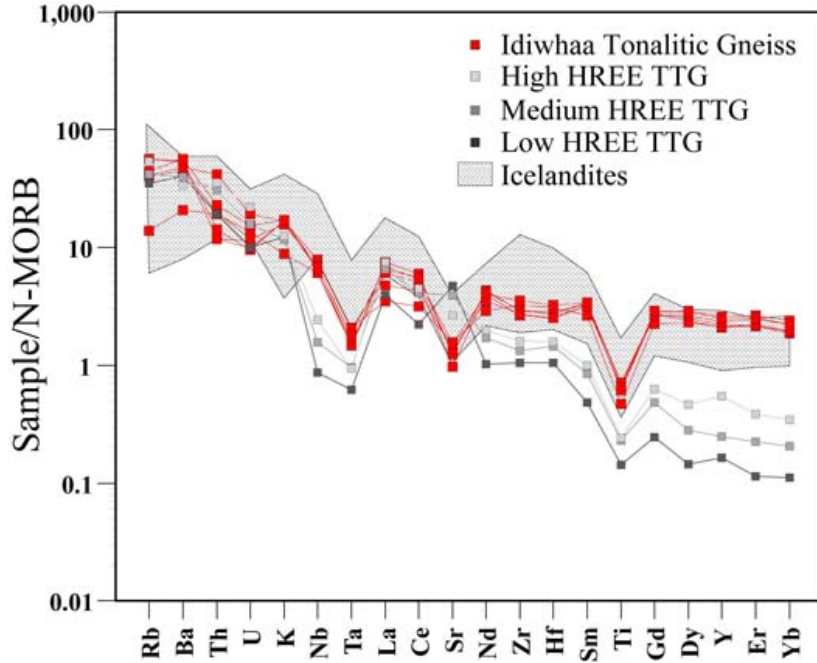


Fig. S4: Trace-element composition of the Idiwhaa Tonalitic Gneiss. Comparison of trace-element composition of Idiwhaa Tonalitic Gneiss with Icelandite and average Archean TTGs. Data sources same as Fig. 1. Note the relative enrichment of the Idiwhaa unit in high-field-strength elements (Hf, Zr, Nb, and Ta) relative to Archean TTG. Samples normalized to ‘normal mid-ocean ridge basalt’⁴¹.

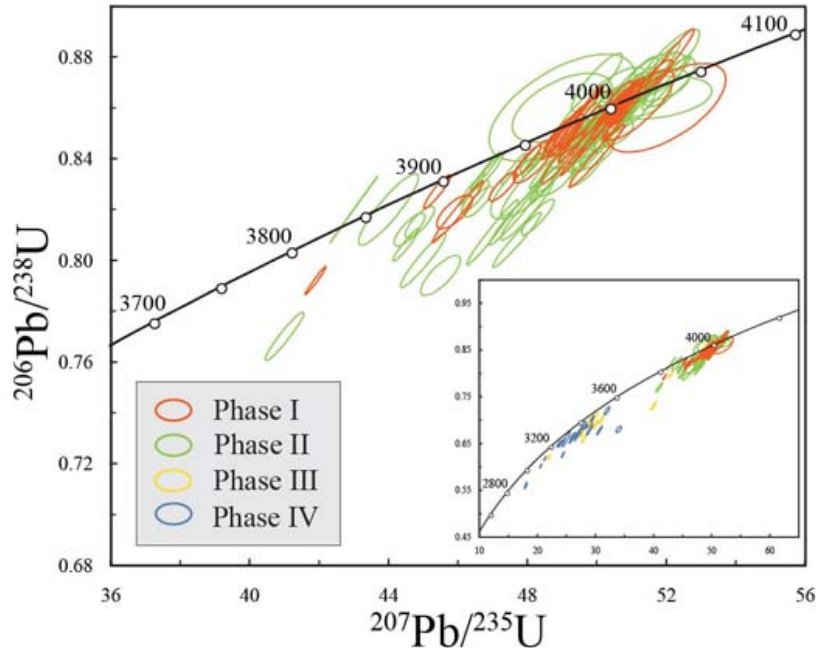


Fig. S5: Concordia plot of older SIMS U-Pb data obtained from Idiwhaa Tonalitic Gneiss sample TC3. The inset plot shows the full dataset including all zircon growth phases. For clarity, uncertainty ellipses are shown at the 1σ level for clarity.

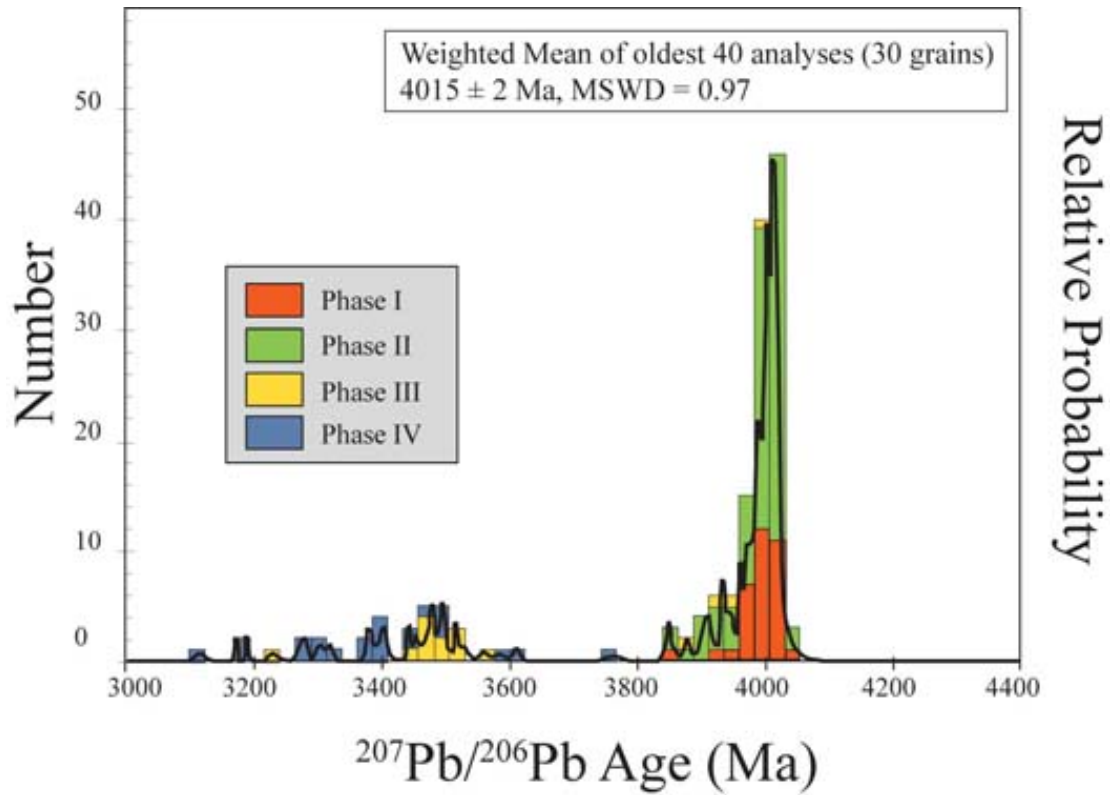


Fig. S6: Probability density plot of $^{207}\text{Pb}/^{206}\text{Pb}$ ages from all TC3 zircon SIMS data. Also shown is a histogram of $^{207}\text{Pb}/^{206}\text{Pb}$ ages, colored according to zircon growth phase. The main peak in relative probability occurs at 4013 Myr and is dominated by Phase I and Phase II zircon, whereas the younger analyses (< 3800 Myr) are exclusively from the two metamorphic domains (Phase III and Phase IV zircon).

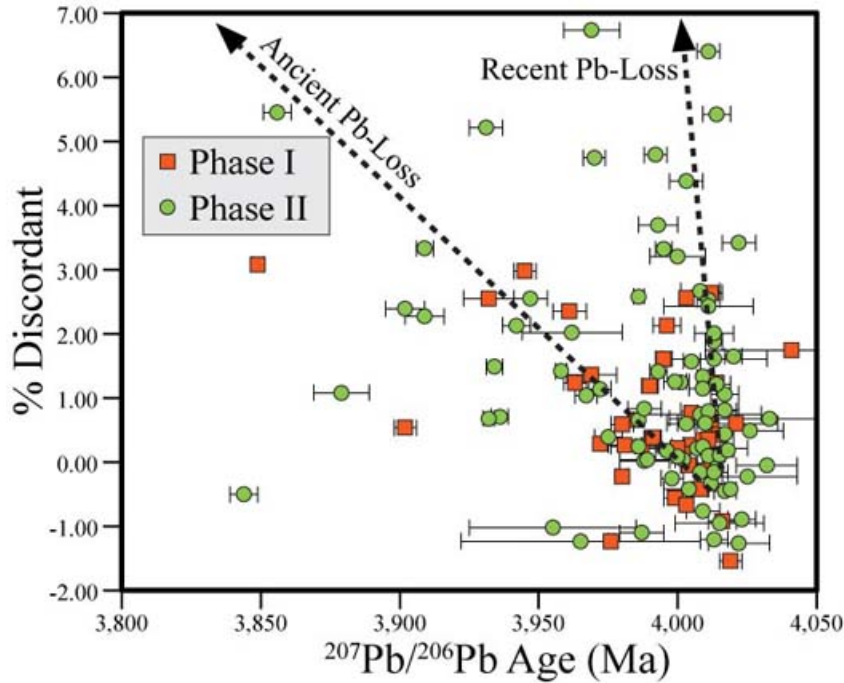


Fig. S7: $^{207}\text{Pb}/^{206}\text{Pb}$ age versus discordancy for Phase I and II zircon (sample TC3). Both zircon domains define two contrasting trends: i) decreasing age with increasing discordance, a sign of ancient Pb-loss; and ii) little change in $^{207}\text{Pb}/^{206}\text{Pb}$ age with increasing discordance, a sign of recent Pb-loss. The majority of all Phase I and II zircon analyses that are $\leq \pm 1\%$ discordant record $^{207}\text{Pb}/^{206}\text{Pb}$ ages > 4000 Myr.

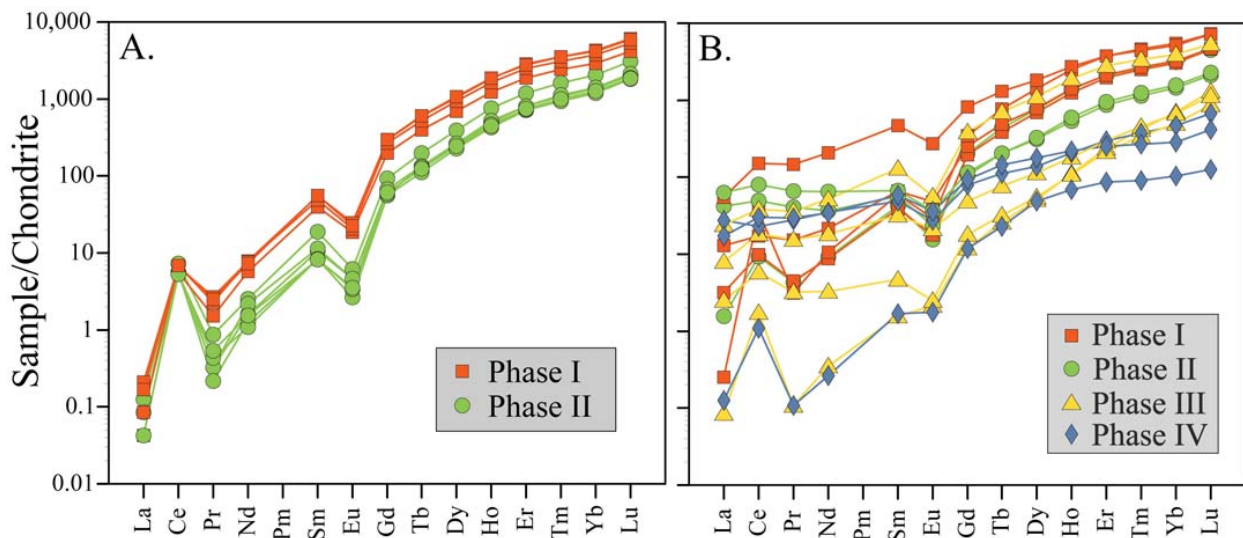


Fig. S8: REE patterns of TC3 zircon. (A) Chondrite normalized 63 plot showing the REE profiles of igneous zircon phases (Phases I and II) with > 4 ppm Ca analyses removed. We attribute the decrease in total REE from Phase I to II zircon to a decrease in the overall REE content of the magma, potentially due to the crystallization of another REE-bearing accessory phase (e.g., titanite). (B) Chondrite normalized 63 REE profiles of analyses with > 4 ppm Ca, which includes analyses of altered Phase I and II zircon and metamorphic growth phases III and IV. Note the flatter

REE profiles of altered igneous and metamorphic growth phases compared to those of unaltered igneous growth phases.

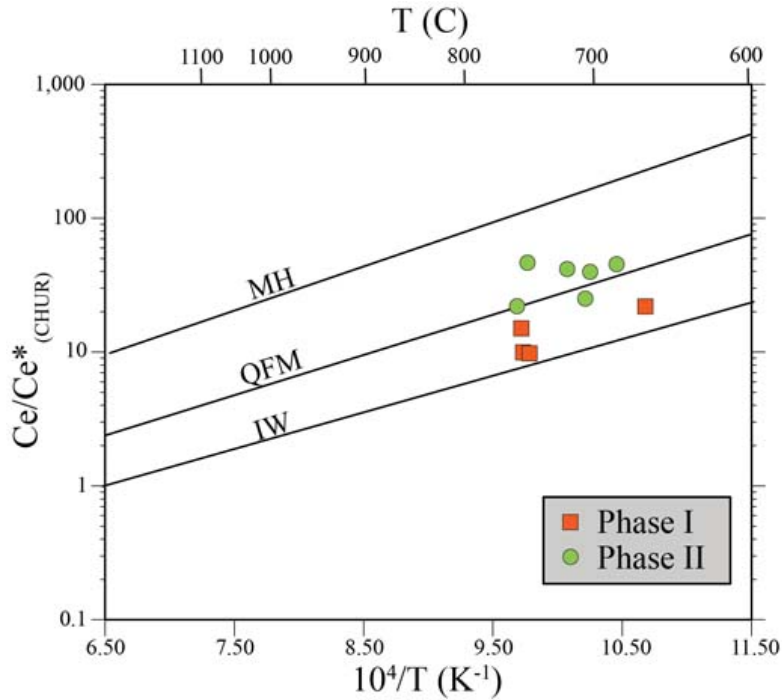


Fig. S9: Magnitude of Ce anomaly versus $10^4/T$ (K^{-1}) for Phase I and II zircon (sample TC3). Shown is a plot of Ce anomaly (Ce/Ce^*) versus inverse temperature for Phase I and II zircon. The Ce anomaly is calculated as $(Ce/Ce^*)_{CHUR} = (C_{eN}) / [(La_N \times Pr_N)^{0.5}]$ where C_{eN} , La_N , and Pr_N are the Ce, La, and Pr concentrations normalized to chondrite⁶³. Temperatures were calculated by Ti-in-zircon thermometry⁴⁶, assuming an activity of TiO_2 in the melt of 0.6. As determined by ref. [29], the plot also shows the magnitudes of Ce anomalies in zircon associated with several common oxygen fugacity buffers (MH = magnetite-hematite; QFM = quartz-fayalite-magnetite; IW = iron-wüstite). Note that at similar Ti-in-zircon temperatures, Phase II zircon is consistently more oxidized (higher Ce/Ce^*) than Phase I.

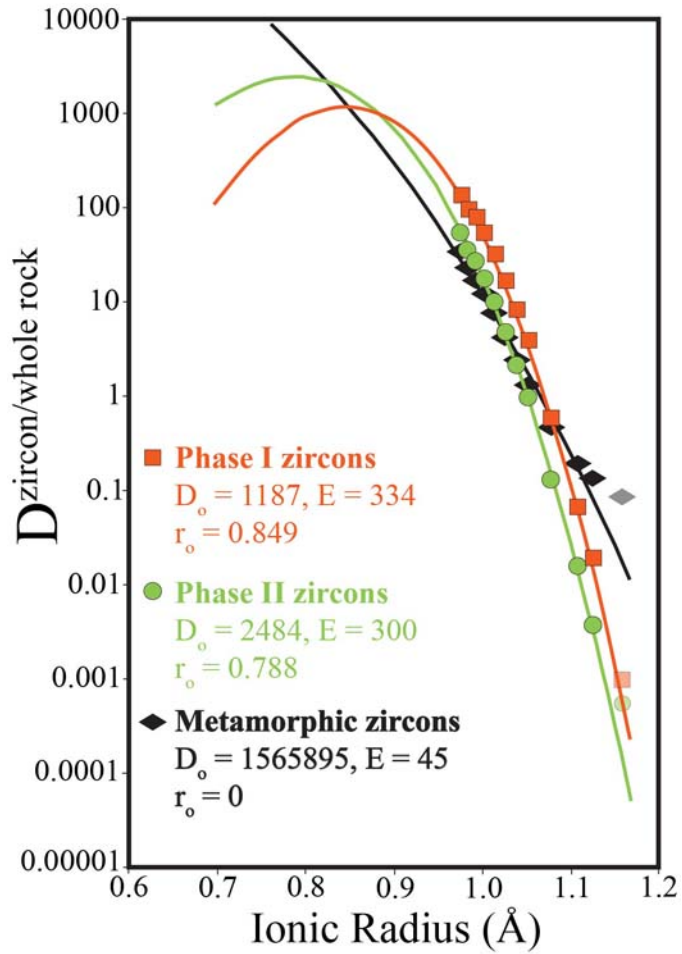


Fig. S10: Onuma plot of REE partition coefficients. Partition coefficients defined by zircon/whole-rock REE values of the Idiwhaa Tonalitic Gneiss (sample TC3), plotted against ionic radii. Each curve represents a fit to the corresponding data using the lattice strain equation of ref. [50]. Eu and Ce (not shown) as well as La (lightly shaded symbols) were excluded from each fit. For each curve, the parameters of the equation used are presented, including the ideal cationic radius (r_0), the theoretical partition coefficient for an ideal cation (D_0), and the Young's Modulus (E). The Phase I and II zircon data both yield plausible solutions to the fit function, whereas average Phase III and IV zircon of metamorphic origin yields a geologically unreasonable solution.

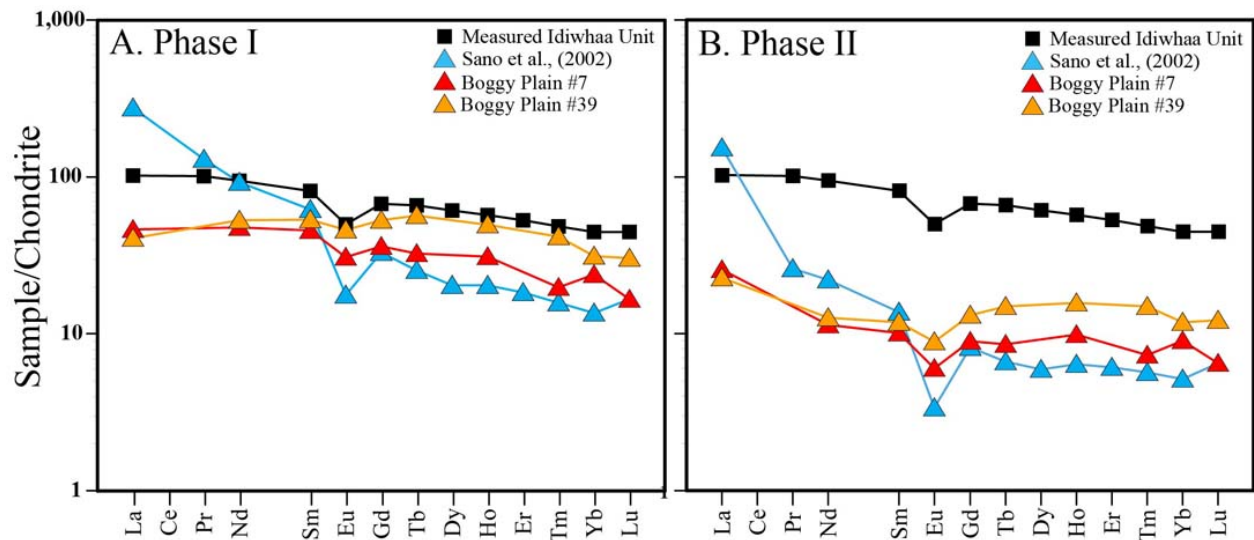


Fig. S11: REE diagrams showing ‘measured’ versus ‘calculated’ whole-rock compositions of the Idiwhaa Tonalitic Gneiss unit (sample TC3). Calculation of REE patterns was carried out assuming the whole-rock was in equilibrium with average Phase I (A) and II (B) zircon. Zircon-whole-rock partition coefficient data used in the calculations are from ref. [52] for a dacite composition and refs. [53–54] for a diorite (BP39) and a granodiorite (BP7) composition. Note that the calculated whole-rock REE patterns for Phase I zircon share many of the features of the measured whole-rock pattern for sample TC3 including relatively low La/Yb, a negative Eu anomaly, and a lack of strong HREE depletion. This suggests that the measured whole-rock patterns of the Idiwhaa Tonalitic Gneiss generally reflect those of its igneous precursor.

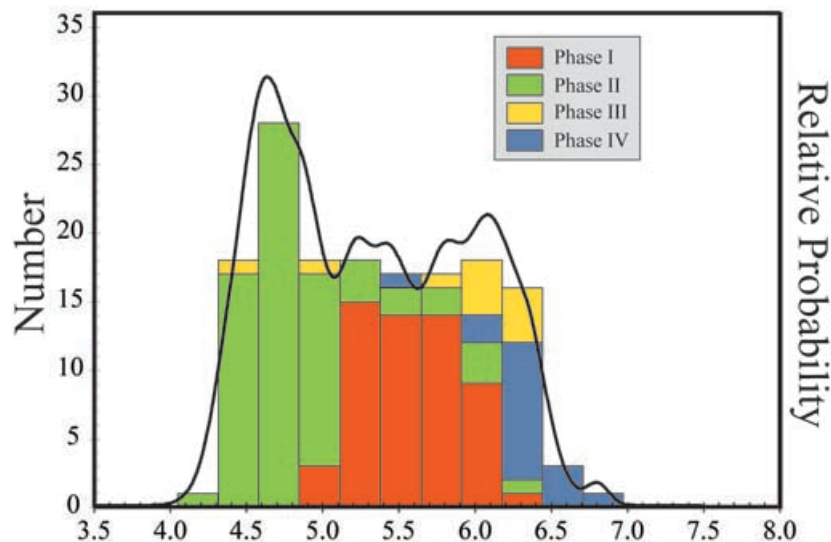


Fig. S12: Probability density plot of zircon oxygen isotopic analyses. Plot includes all 155 oxygen isotopic analyses from ITG unit zircons (sample TC3) excluding one analysis of highly altered zircon material which is reported in Table S3. Histogram colors correspond to zircon growth phases. Note that this plot contains all the

measured oxygen isotope compositions, whereas Fig. 2C only shows the data for analytical spots for which both oxygen and U-Pb isotopic compositions were determined.

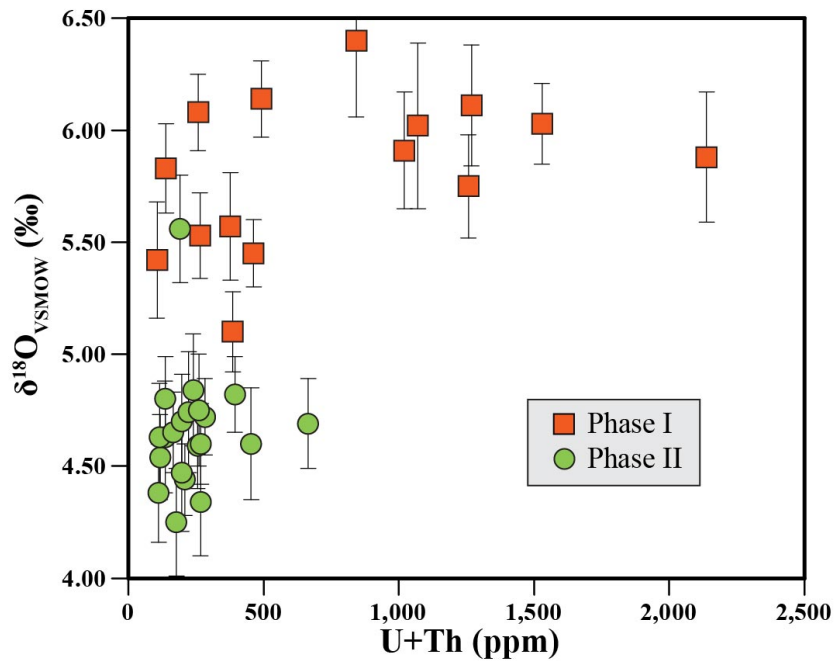


Fig. S13: $\delta^{18}\text{O}$ versus U+Th contents in Phase I and II zircons. Overall, Phase I zircon contains significantly more U and Th than Phase II zircons. It follows that Phase I zircon would accumulate radiation damage more quickly than Phase II so that at the time of zircon recrystallization, ~3.2 Ga, Phase I cores were be more susceptible to overprinting. This is confirmed in the SEM and CL images of many Phase I zircons, and is highlighted in Fig. 2B. This later recrystallization may preferentially overprint the O-isotope ratio of some Phase I zircons. We suggest that some Phase I igneous cores may have been overprinted by later metamorphic fluids, causing their $\delta^{18}\text{O}$ values to be elevated above 6‰.